Available online at www.sciencedirect.com
ScienceDirect
Trans. Nonferrous Met. Soc. China 35(2025) 3761−3777
Transactions of Nonferrous Metals Society of China
www.tnmsc.cn

Simultaneously improving intermediate-temperature strength and ductility of Ni−Co-based superalloy by tailoring high-density stacking faults

Yu-bi GAO[1,2], Xing-mao WANG[1,2], Jia-yu XU[1,2], Bo LIU[1,2], Bing ZHEN[1,2], Yu-tian DING[1,2], Bin GAN[3], Ting-biao GUO[1,2], Jun-zhao LIU[1,2]

1. School of Materials Science and Engineering, Lanzhou University of Technology, Lanzhou 730050, China;
2. State key Laboratory of Advanced Processing and Recycling of Non-ferrous Metals, Lanzhou University of Technology, Lanzhou 730050, China;
3. Beijing Key Laboratory of Advanced High Temperature Materials, Central Iron & Steel Research Institute, Beijing 100081, China

Received 12 March 2024; accepted 13 November 2024

Abstract: High-density stacking faults (SFs) were introduced into a novel Ni−Co-based superalloy through warm rolling at 300−500 °C, and the effects of SFs on its tensile properties at intermediate temperatures (650 and 750 °C) were investigated. The results indicated that all warm rolled specimens have high-density SFs and Lomer−Cottrell locks compared with the initial specimens. Meanwhile, the simultaneous improvement of intermediate-temperature strength and ductility of alloys can be achieved by high-density SFs. In particular, the specimen rolled at 300 °C exhibited a superior combination of high strength (yield and ultimate tensile strengths of (1311±18) and (1462±25) MPa respectively at 650 °C, and (1180±17) and (1293±15) MPa respectively at 750 °C) and high fracture elongation ((26.7±2.5)% at 650 °C and (10.7±1.3)% at 750 °C). The high strengths and facture elongations of all warm-rolled specimens were primarily attributed to the interaction of pre-existing γ' phases, high-density SFs and Lomer−Cottrell locks with dislocations, as well as to the formation of high-density deformation nano-twins during tensile loading.

Key words: Ni−Co-based superalloy; warm rolling; stacking fault; Lomer−Cottrell lock; deformation nano-twins; mechanical properties

1 Introduction

Ni-based wrought superalloys are widely used to fabricate turbine disks in aircraft engines owing to their excellent high-temperature strength, oxidation resistance, creep resistance, and fatigue properties [1−4]. However, these alloys generally exhibit low intermediate-temperature ductility or embrittlement in the 500−900 °C service temperature range; that is, their tensile plasticity decreases significantly, detrimentally affecting their processibility and service properties [5−7]. The simultaneous improvement of the intermediate-temperature strength and ductility may represent a starting point for finding a method to eliminate the poor ductility or embrittlement of Ni-based wrought superalloys at such temperatures.

Over the past few decades, many researchers have simultaneously improved the high-temperature strength and ductility of Ni-based wrought superalloys through alloying [8−12], increasing grain boundary strengthening [13−15], and microstructural tailoring [16−18] to eliminate poor ductility or

Corresponding author: Yu-bi GAO, Tel: +86-15101262736, E-mail: gaoyubi1991@126.com, gaoyubi1991@lut.edu.cn;
Yu-tian DING, Tel: +86-13893243521, E-mail: dingyutian@126.com, dingyt@lut.edu.cn
https://doi.org/10.1016/S1003-6326(25)66911-1

embrittlement. These studies have proven that reducing the stacking fault (SF) energy by adding Co can change the deformation mechanisms of Ni-based wrought superalloys, thereby simultaneously improving strength and ductility at intermediate temperatures (725−800 °C) [8−10]. However, alloys with an excessive Co content exhibit considerably decreased strength and/or ductility at higher temperatures [19,20]. ZHU et al [11] reported that the addition of Ta simultaneously improved the ultimate tensile strength and uniform elongation of a Ni−Co-based superalloy at 760 °C owing to the combined effects of increased grain boundary strength, reduced critical shear stress, and promoted twinning deformation. LIU et al [12] found that an increase in N content had little effect on the yield and ultimate tensile strengths of a Ni−Fe-based wrought superalloy at 750 °C; however, it increased ductility of the superalloy remarkably. Furthermore, the grain boundary strength of a Ni-based C-276 alloy was improved by long-term aging, causing simultaneous increase in yield strength, ultimate tensile strength, and elongation at 700 °C [13]. Similarly, the tensile elongation of the GH4065A superalloy at 700 °C was significantly improved by long-term aging, but its tensile strength was slightly reduced [14]. YANG et al [15] proposed a duplex aging strategy to efficiently realize grain boundary stabilization, thereby significantly improving the tensile strength and plasticity of an $L1_2$-strengthened Ni−30Co−13Fe−15Cr−6Al−6Ti−0.1B (at.%) high-entropy alloy at 700 °C. In addition, a novel ε-plate/nano-twin structure has been tailored to provide satisfactory high-temperature strength–ductility synergy and structural stability of a NiCrCo-based alloy after aging, leading to a yield strength enhancement of ~98% at 700 °C while maintaining reasonable ductility [16]. Finally, tailoring the annealing twins and twin boundaries (TBs) synchronously improved the high- temperature strength and ductility of an FeMnCoCr high-entropy alloy [17] and Cu−16Al (at.%) alloy [18]. Therefore, tailoring the twins or SFs of stable structures through processing represents an attractive approach to simultaneously improving the intermediate-temperature strength and ductility of Ni-based wrought superalloys.

Recent studies [21,22] have found that inducing high-density deformation twins (DTs) and SFs in Ni−Co-based superalloys using a pre-creep treatment and pre-tensile loading treatment, respectively, significantly improved their yield strengths at 760 °C but significantly reduced their uniform elongations. WANG et al [23] reported that pre-existing high-density nano-twins significantly improved the strength and maintained the excellent ductility of a novel Ni−Co-based superalloy at room temperature. The SF is a transitional plane defect that can be converted into twin structures to provide similar strengthening and toughening of face-centered cubic metals as TB structures. However, the effects of high-density SFs on the mechanical properties of such metals have received less attention than those of TBs. Thus, in this study, a warm-rolling (WR) pre-treatment was used to induce high-density SFs in a novel Ni−Co-based superalloy. The tensile mechanical properties of the resulting specimens were evaluated at 650 and 750 °C and compared with those of a standard heat-treated specimen. The results of this comparison were analyzed to determine the reasons for the increased alloy strength and ductility. Thus, this study provides a new strategy for efforts to eliminate intermediate- temperature embrittlement of Ni-based superalloys.

2 Experimental

2.1 Material preparation

The base material used in this study comprised forged rods made of a novel Ni−Co-based superalloy with the following chemical composition: Ni−20.0Co−16.5Cr−5.0W−2.5Al−2.5Ti−2.5Nb−0.02C (wt.%). Superalloy ingots were cast using the vacuum induction melting and electroslag remelting processes, then homogenized and forged into 150 mm diameter rods. The forged rods were solution-treated at 1080 °C for 2 h followed by air cooling (AC) at room temperature (~22 °C). WR was subsequently conducted on the solution-treated (ST) rod specimens to realize a thickness reduction of 45% at 300, 400, and 500 °C, labelled as Specimens WR-300, WR-400, and WR-500, respectively. Thereafter, two-step or double aging (DA) was conducted on all specimens at 650 °C for 24 h, then at 760 °C for 16 h+AC, as shown in Fig. 1(b). For comparison, an ST specimen without

WR pre-treatment was also subjected to DA, as shown in Fig. 1(a); this specimen is referred to as the "initial specimen".

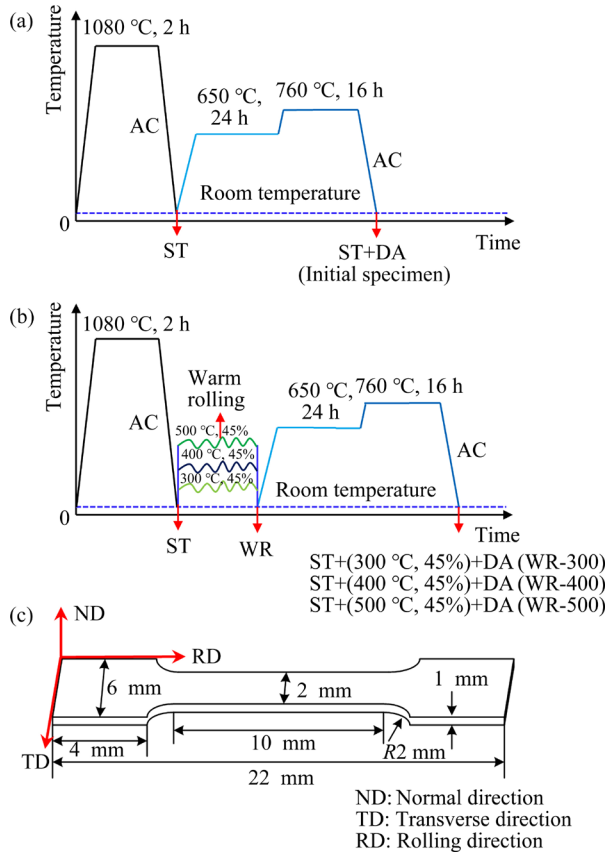

Fig. 1 Schematic diagrams of thermomechanical treatment and tensile specimens of Ni−Co-based wrought superalloy: (a) Solution treatment and two-step aging; (b) Solution treatment and pre-warm rolling and two-step aging; (c) Dimensions of tensile specimens

2.2 Mechanical property tests

Tensile testing specimens with 1 mm in thickness, 2 mm in gauge width, and 10 mm in gauge length were machined along the rolling direction (or length direction) of the initial specimen, WR-300, WR-400, and WR-500, as shown in Fig. 1(c). All faces of the specimen gauge sections were subsequently ground using 400-grit SiC sandpaper. Finally, the tensile tests were conducted at 650 and 750 °C by applying a constant strain rate of 0.2 mm/min until specimen rupture using an LE5105 electronic universal testing machine equipped with a video extensometer. The reported ultimate tensile strength (UTS), yield strength (YS), and facture elongation (ε_f) of each specimen were obtained as the average result of three tests.

2.3 Microstructure characterization

Microstructural observations of the pre- and post-tensile test specimens were obtained through electron backscatter diffraction (EBSD), scanning electron microscopy (SEM), transmission electron microscopy (TEM), and selected area electron diffraction (SAED). For the EBSD analysis, specimens collected before and after the tensile tests were mechanically polished, then electro-polished in a mired solution of 5 vol.% $HClO_4$ and 95 vol.% C_2H_5OH at 30 V and 0 °C and for 30−40 s. The EBSD maps were subsequently obtained at a voltage of 20 kV and a step size of 1 μm using a Gemini 300 FEG-SEM system equipped with an Oxford C-swift EBSD detector; the results were analyzed using the HKL CHANNEL 5.0 software. The specimens for SEM were mechanically polished, then electrochemically etched in a mixed solution of 10 vol.% $HClO_4$ and 80 vol.% C_2H_5OH at 10 V and room temperature (22 °C) for 30 s. The SEM operating voltage was set to be 20 kV. Specimens collected before and after the tensile tests were subjected to TEM analysis using an FEI Talos F200 TEM system operated at 200 kV to examine their microstructures and deformation mechanisms. The TEM specimens collected after the tensile tests were cut from the deformed test specimens, carefully ground to a thickness of 50 μm, and then subjected to ion thinning using a Gatan 695 precision ion polishing system.

3 Results

3.1 Microstructure evolution

Figure 2 shows the EBSD inverse pole figures and corresponding grain boundary and geometrically necessary dislocation (GND) density (ρ^{GND}) maps of the alloy specimens after WR at different temperatures. In Figs. 2(a_2−d_2), the grey lines represent low-angle grain boundaries (LAGBs) with misorientations of 2°−15°, black lines represent high-angle grain boundaries (HAGBs) with misorientations greater than 15°, and red lines represent TBs with an ideal misorientation of 60°/⟨111⟩. In the initial specimen, the microstructure consisted of fine and coarse equiaxed grains with random orientations as well as many lamellar annealing twins (Fig. 2(a_1)). This specimen exhibited a low average GND density (2.41×10^{14} m^{-2} in Fig. 2(a_3)), which indicated that

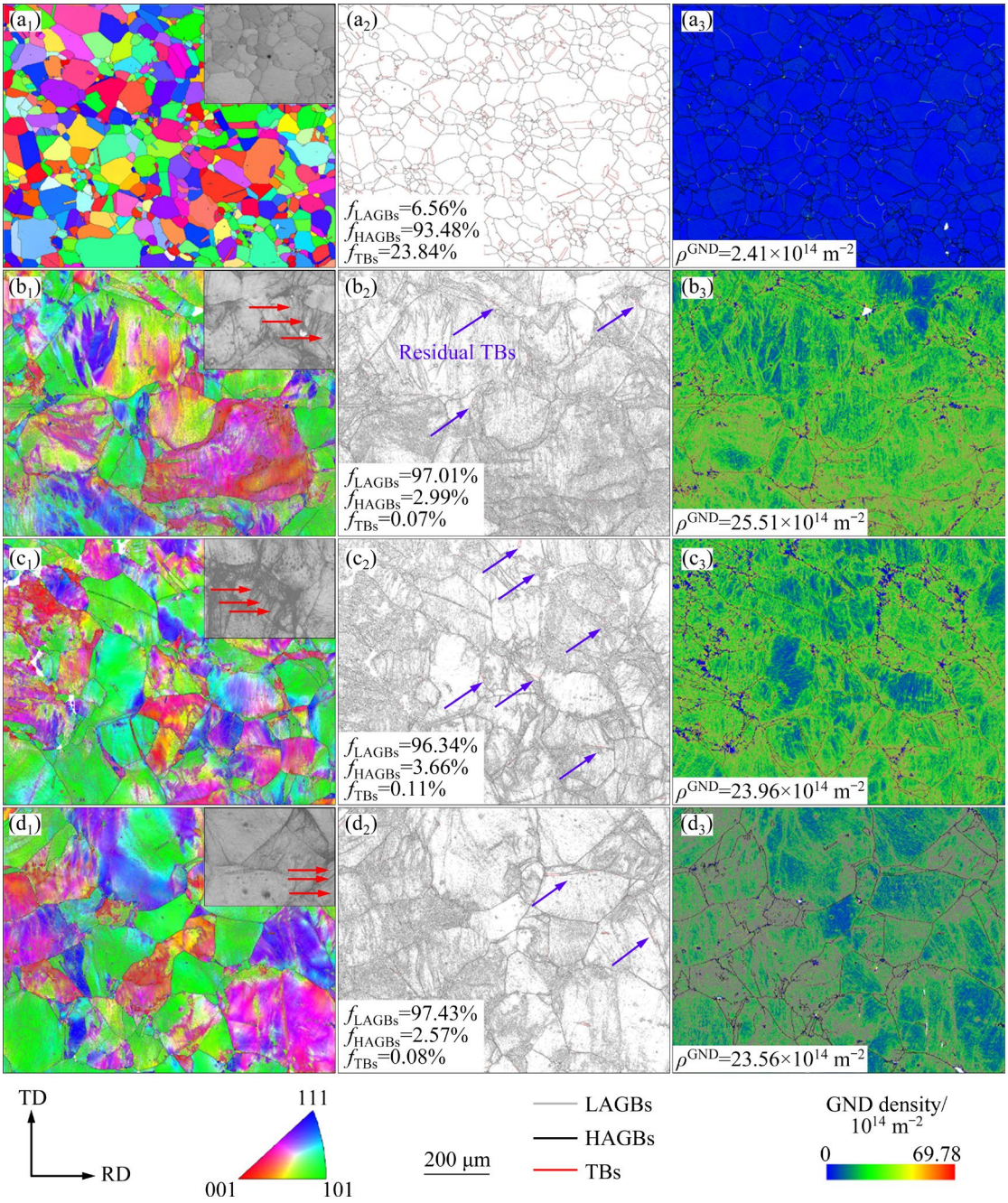

Fig. 2 EBSD inverse pole figure (a_1−d_1), grain boundary (a_2−d_2), and GND density (a_3−d_3) maps of alloy specimens during WR at different temperatures: (a_1−a_3) Initial specimen; (b_1−b_3) 300 °C; (c_1−c_3) 400 °C; (d_1−d_3) 500 °C (Insets in (a_1−d_1) are OM images, and corresponding slip traces are indicated by red arrows; Residual annealing TBs are indicated by blue arrows in (b_2−d_2))

the solution treatment after hot forging induced full recrystallisation and grain growth accompanied by the formation of annealing twins [24]. The microstructures of the specimens after WR pre-treatment at different temperatures consisted of coarsely deformed grains and a few residual annealing twins (Figs. 2(b_2−d_2)), with parallel slip traces appearing within the coarse deformed grains (insets in Figs. 2(a_1−d_1)). Figures 2(a_2−d_2) show that HAGBs dominated in the initial specimen, whereas LAGBs dominated in the WR specimens. During WR at different temperatures, the dislocations that accumulated near the annealing TBs reacted with them, causing the latter to gradually lose coherence and transform into random HAGBs, subsequently transforming the HAGB absorption dislocations into LAGBs [25]. This mechanism explains the observed change of HAGBs into LAGBs and

confirms the disappearance of a large quantity of annealing TBs during WR deformation regardless of temperature. These changes significantly increased the GND density of each WR specimen; however, the GND density slightly decreased with increasing WR temperature (Figs. 2(b_3−d_3)).

The deformation structures of the WR specimens subjected to different rolling temperatures were characterized through TEM. Figure 3 shows the typical microstructures of the initial and WR specimens. In Fig. 3(a) and the corresponding SAED pattern, annealing twins can be clearly observed in the initial specimen. Meanwhile, the morphologies of γ' phase in the initial specimen consisted of the spherical coarse primary γ', uniform secondary γ', and fine tertiary γ' phases, as shown in Fig. 3(b). In addition, the EDS line and map scanning analyses of γ and γ' phases in STEM mode show that the spherical γ' phase is rich in Ni, Al, and Ti elements, and the γ matrix is rich in Ni, Co, and Cr elements, as shown in Fig. 4. Figures 3(c, d) show a significant quantity of dislocations (green arrow) and SFs (red and blue arrows) in the γ matrix or γ' phase of WR-300. Furthermore, the high-resolution TEM (HRTEM) image and the corresponding fast Fourier transform (FFT) pattern in Fig. 3(e) show a considerable quantity of Lomer−Cottrell (L−C) locks (red dots) in WR-300. The number of SFs (red and blue arrows) and L−C locks in the alloy increased

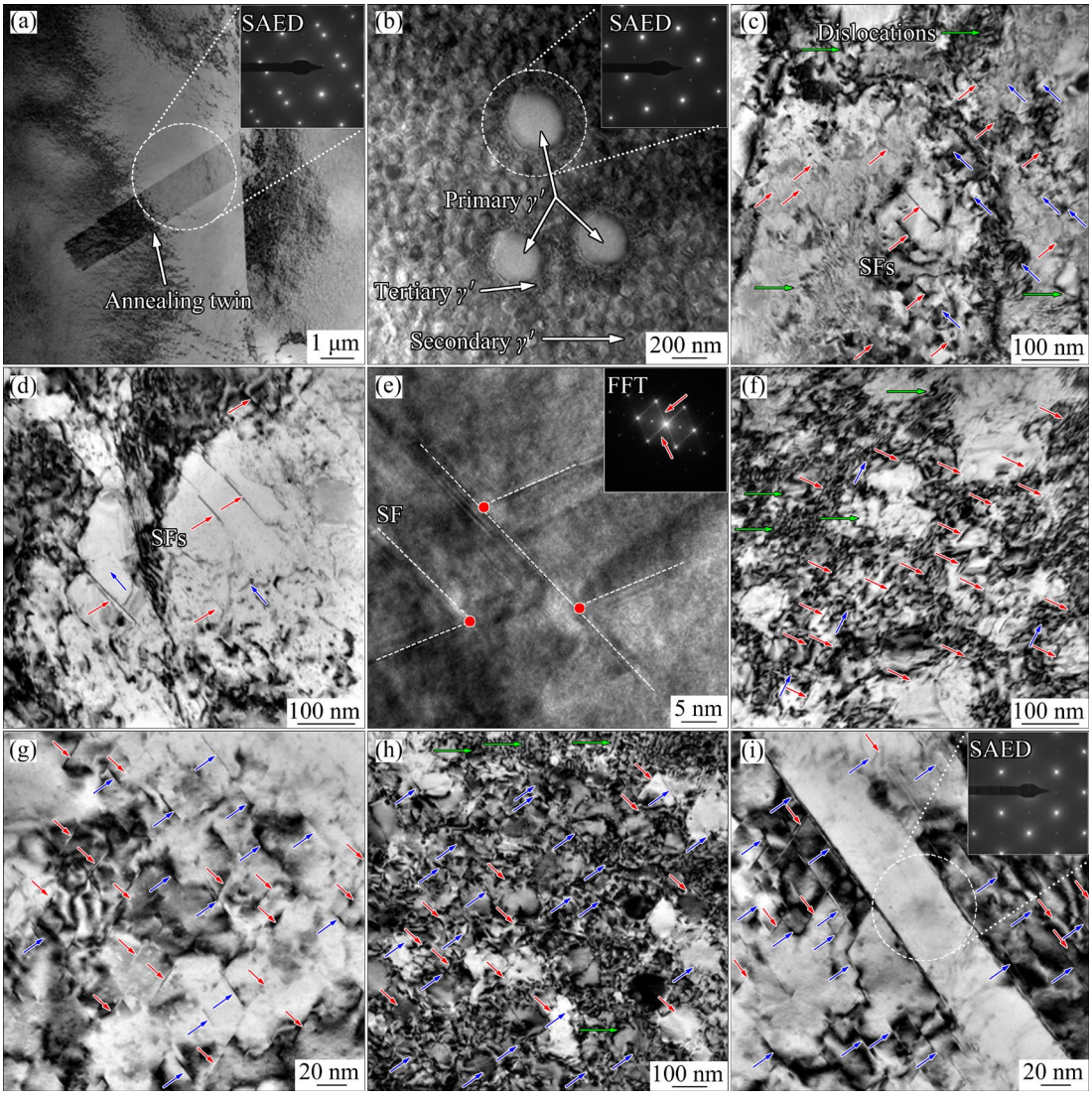

Fig. 3 TEM and HRTEM images of initial and WR specimens: (a, b) Low- and high-magnification TEM images of initial specimen, respectively; (c, d) Low- and high-magnification TEM images of WR-300, respectively; (e) HRTEM image showing SF network (white dash line) and L−C locks (red dot) in (d); (f, g) Low- and high-magnification TEM images of WR-400, respectively; (h, i) Low- and high-magnification TEM images of WR-500, respectively

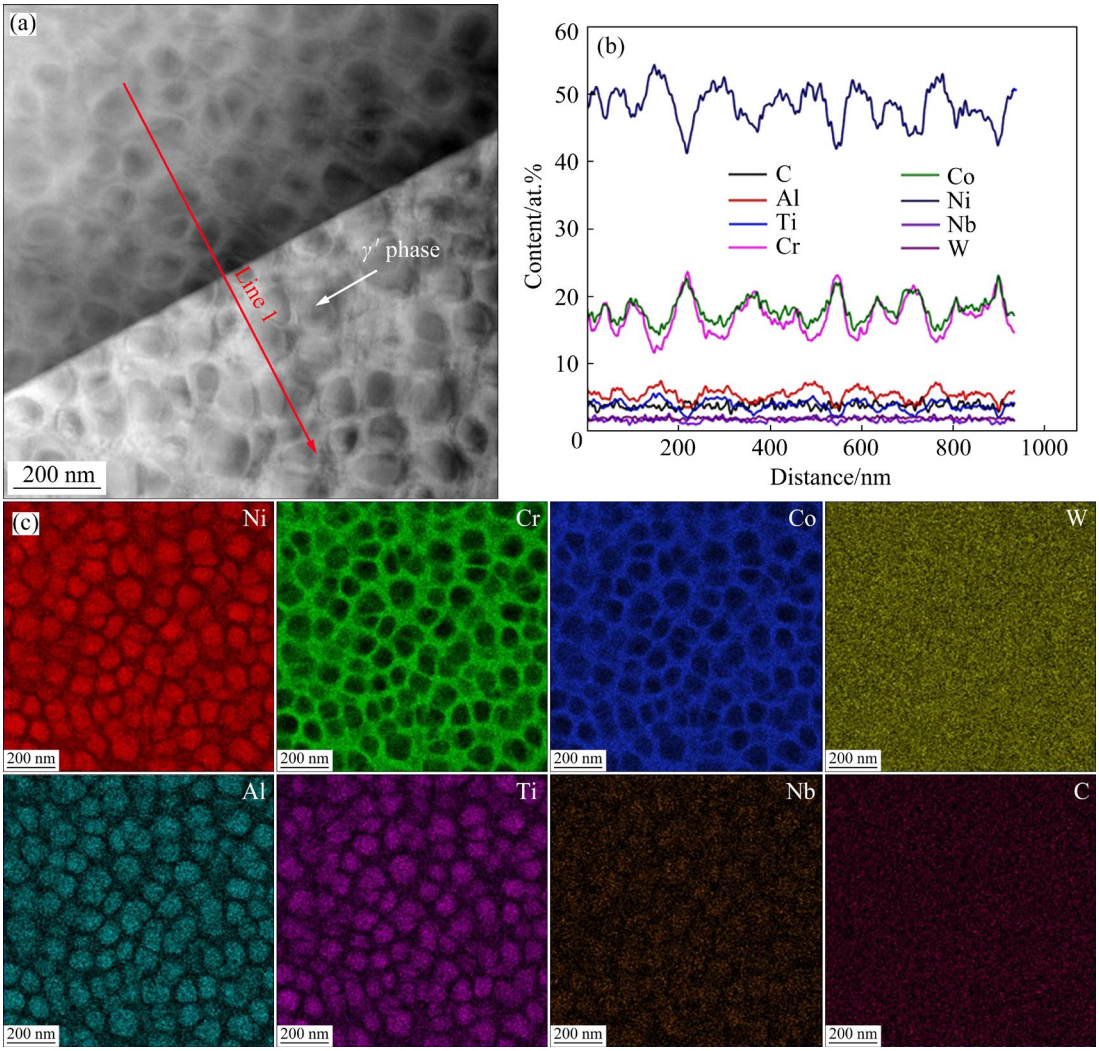

Fig. 4 HAADF−STEM image of initial specimen and corresponding line and map scanning analysis results: (a) HRAADF−STEM image of γ' phases in initial specimen; (b) Line scan analysis results of Line 1 in (a); (c) Map scanning analysis results in (a)

(Figs. 3(f−h)) as the WR temperature increased, whereas the GND density slightly decreased (Figs. 2(b_3−d_3)). Moreover, Fig. 3(i) and the corresponding SAED pattern show that the lath structure was not a DT. These results indicated that the planar SF-dominated deformation mode occurred during WR pre-treatment at different temperatures.

3.2 Tensile properties

Figures 5(a, d) show the engineering stress–strain curves obtained by tensile testing of the initial and WR specimens at 650 and 750 °C, respectively. Clearly, the engineering stress–strain curve of the initial specimen exhibited a continuous work-hardening trend, whereas those of the WR specimens initially exhibited work hardening up to the ultimate tensile strength, and then showed a work softening trend; this may be related to the initial microstructure and tensile deformation mechanism of the specimens under the test temperatures. Meanwhile, the initial specimen exhibited lower strengths (YS=(929±11) MPa and UTS=(1104±20) MPa at 650 °C; YS=(909±9) MPa and UTS=(949±11) MPa at 750 °C) and facture elongations (ε_f=(3.2±0.5)% at 650 °C; ε_f=(0.8±0.2)% at 750 °C) than the WR specimens. Notably, the strength and facture elongation of the alloy at 650 and 750 °C were significantly improved after WR regardless of the applied temperature (Figs. 5(a, d)). These results indicated that WR improved the strength of alloy and increased its facture elongation

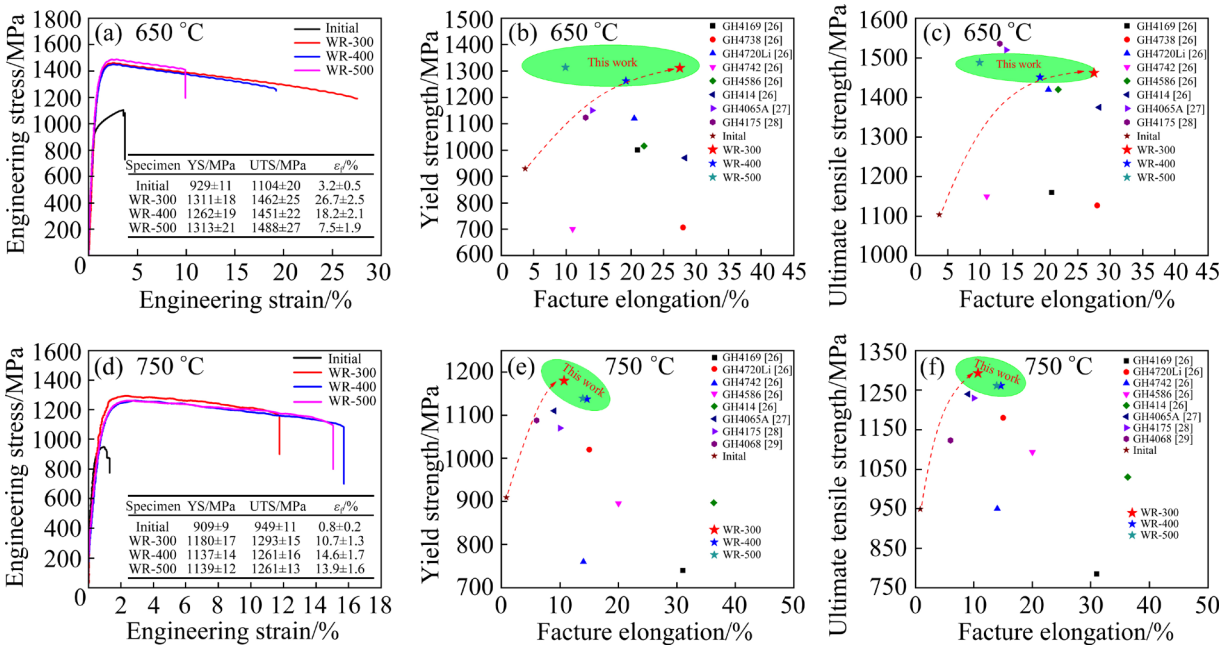

Fig. 5 Tensile mechanical properties of initial and warm-rolled specimens at 650 and 750 °C, respectively, and comparison with tensile mechanical properties of some typical Ni-based disc superalloys [26−29]

when subjected to tension at 650 and 750 °C. These improvements are closely related to the initial microstructure and tensile deformation mechanism of the alloy. Comparing the Ni-based superalloys in Figs. 5(b, c, e, f), a general trade-off can be observed between the yield/ultimate tensile strengths and facture elongations of the specimens, with the WR-300 specimen exhibiting an advantageous combination of high strength and ductility when tested at 650 and 750 °C.

3.3 Fracture behavior

Fracture always occurs in the weakest part of a material, and fracture morphologies reflect considerable valuable information describing the tensile failure process. Figures 6 and 7 depict the typical morphologies of the fracture surface and fracture cross-sections, respectively, in the initial and WR specimens tested at 650 and 750 °C. When the initial specimen was tested at 650 °C, several dimples, carbides, and secondary cracks as well as a number of quasi-cleavage fractures and ductile intergranular tears were observed on its fracture surface, as shown in Figs. 6(a, a_1, a_2); the corresponding fracture cross-section morphology (Fig. 7(a)) indicated that the fracture mechanism was mixed mode of intergranular and transgranular fractures. However, when tested at 750 °C (Figs. 6(e, e_1, e_2) and Fig. 7(e)), the initial specimen exhibited the intergranular cracking fracture mechanism. Thus, the fracture mode of the initial specimen transformed from a mixed mode of intergranular and transgranular fractures to a purely intergranular fracture mode likely owing to the weakening of grain boundary strength with increasing test temperature. These results are consistent with those shown in Figs. 5(a, d); with an increase in the tensile test temperature, the fracture elongation of the initial specimen decreased.

The fracture morphology of the alloy changed significantly with WR temperature when tested at 650 and 750 °C. When tested at 650 °C, a lower WR temperature corresponded to a decrease in ductile intergranular tears and micro-pores and an increase in dimples, although carbides and secondary cracks still existed in the fracture surfaces of the alloy, as shown in Figs. 6(b−d). However, when tested at 750 °C, a higher WR temperature corresponded to a decrease in the intergranular cracks and an increase in dimples, whereas carbides and ductile quasi-cleavage fractures as well as ductile intergranular tears still existed in the fracture surfaces of the alloy, as shown in Figs. 6(e−h). Together with the corresponding fracture cross-section morphologies in Figs. 7(b−d) and (f−h), it was suggested that WR

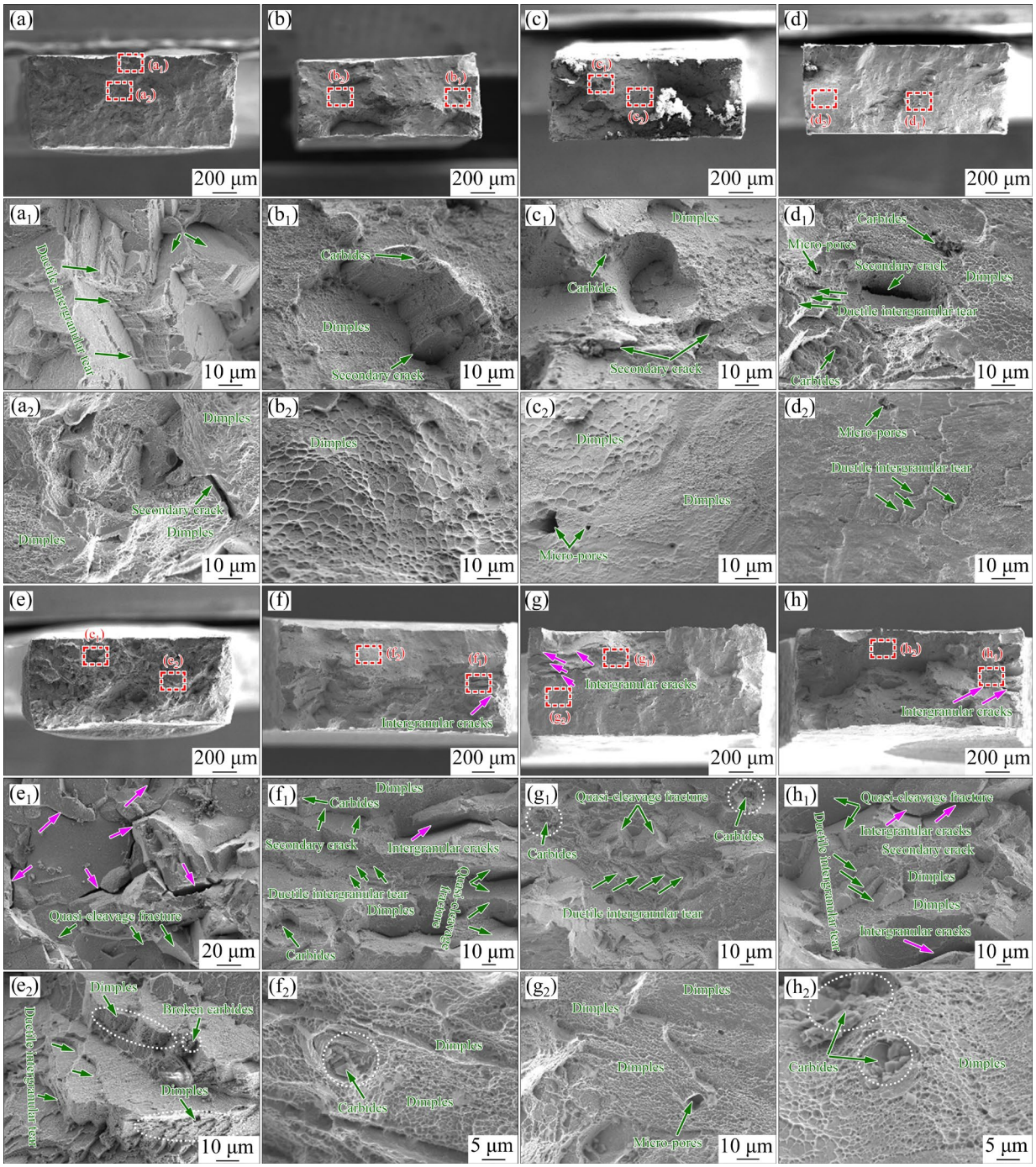

Fig. 6 Fracture surface morphologies of initial and warm-rolled specimens at different tensile temperatures: (a, a_1, a_2) Initial specimen at 650 °C; (b, b_1, b_2) WR-300 specimen at 650 °C; (c, c_1, c_2) WR-400 specimen at 650 °C; (d, d_1, d_2) WR-500 specimen at 650 °C; (e, e_1, e_2) Initial specimen at 750 °C; (f, f_1, f_2) WR-300 specimen at 750 °C; (g, g_1, g_2) WR-400 specimen at 750 °C; (h, h_1, h_2) WR-500 specimen at 750 °C

deformation did not change the fracture mechanism of the alloy significantly when it was tested at 650 °C, remaining the mixed intergranular and transgranular fracture but significantly increased the prevalence of dimples, whereas the fracture mechanism of the alloy when tested at 750 °C transformed from the intergranular fracture to the mixed intergranular and transgranular fracture. These results are consistent with those presented in Figs. 5(a, d), indicating that the fracture elongation of the alloy increased significantly after WR deformation when tested at 650 and 750 °C.

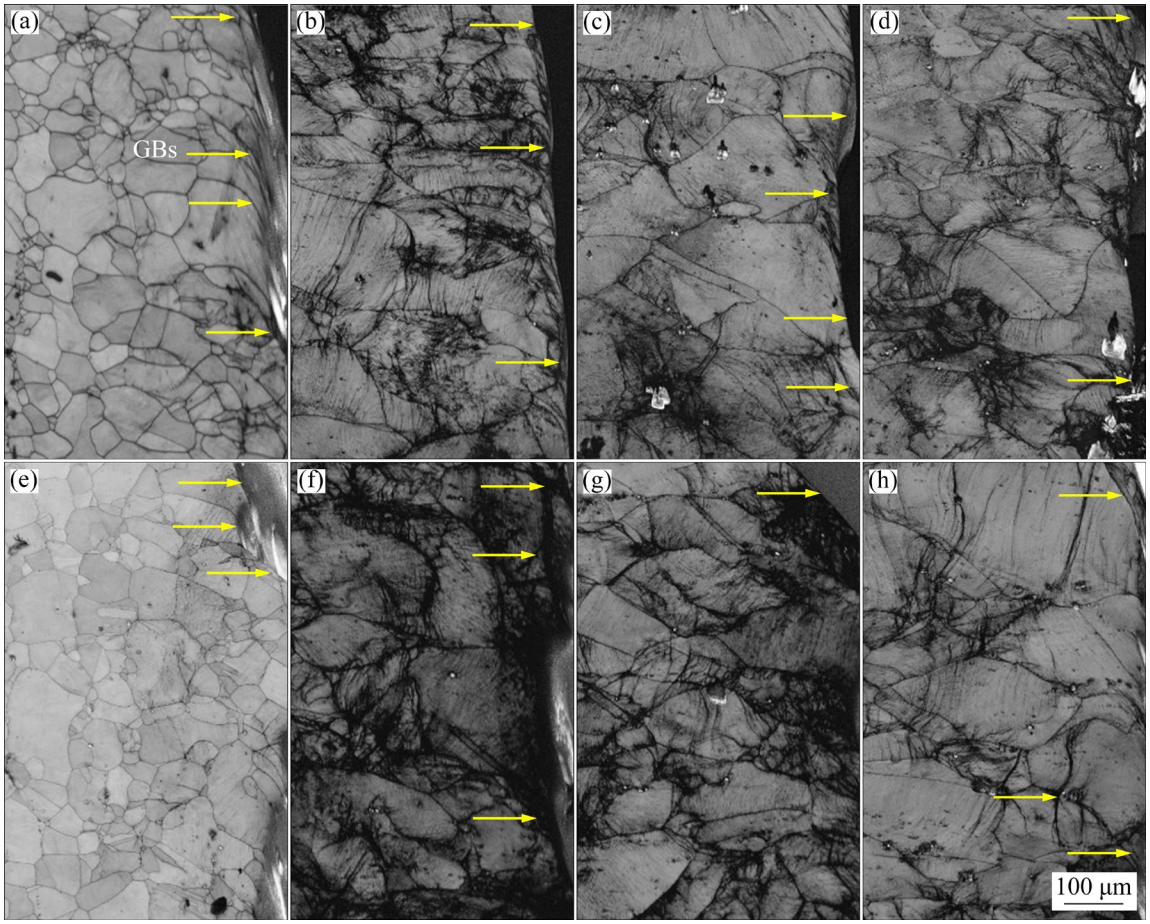

Fig. 7 Cross-section facture morphologies of initial and warm-rolled specimens at different tensile temperatures: (a, e) Initial specimen; (b, f) WR-300 specimen; (c, g) WR-400 specimen; (d, h) WR-500 specimen; (a−d) 650 °C; (e−h) 750 °C

3.4 Deformation mechanism

The deformation mechanisms of the initial and WR specimens during tensile deformation at 650 and 750 °C were characterized using the EBSD and TEM results obtained after tensile fracture. Figures 8 and 9 show the EBSD-obtained GND density maps of the initial and WR specimens after tensile failure at different temperatures. Clearly, the GND density of the initial specimen increased after tensile deformation at both 650 and 750 °C (Fig. 2(a_3), Figs. 8(a, d), and Fig. 9), indicating that it experienced work hardening during tensile deformation; this result is consistent with the tensile engineering stress–strain curve for the initial specimen in Figs. 5(a, d). However, the GND densities of the WR specimens tested at different temperatures decreased after tensile deformation at 650 and 750 °C (Figs. 2(b_3−d_3), Figs. 8(b−d), Figs. 8(f−h), and Fig. 9), indicating that work softening occurred; this result is consistent with the tensile engineering stress–strain curves of the WR specimens tested at different temperatures in Figs. 5(a, d). The work softening phenomenon exhibited by all the WR specimens during tensile deformation at 650 and 750 °C is likely related to the interaction between SFs and dislocations [30].

Figure 10 shows the TEM and HRTEM images of the initial and WR-300 specimens after tensile deformation at 650 and 750 °C. When tested at 650 °C, a significant quantity of slip bands and SFs were observed in the initial specimen (Figs. 10(a, a_1)), and many paired dislocations were present inside the slip bands that sheared the γ matrix and γ' phases, as shown in the inset of Fig. 10(a). In addition, many SFs also sheared the γ matrix and γ' phases (Fig. 10(a_1)), and the SFs of different {111} slip planes intersected to form L−C locks (inset in Fig. 10(a_1)). These results indicated that the deformation of the initial specimen tested at 650 °C was dominated by dislocation pairs and

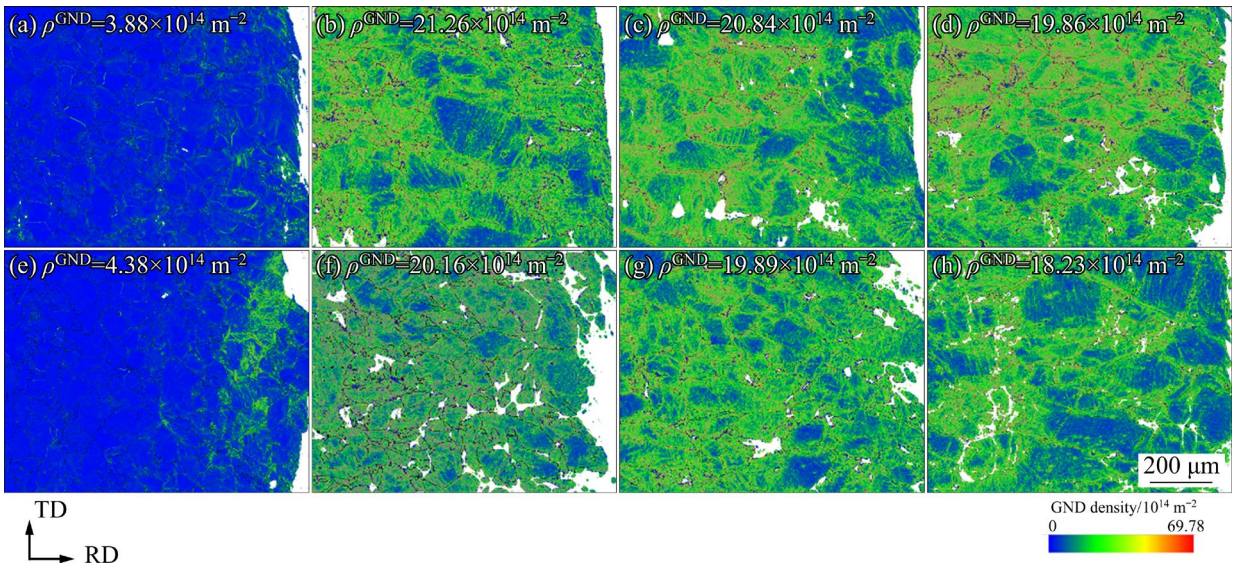

Fig. 8 GND density maps of initial and warm-rolled specimens after tensile failure at 650 and 750 °C: (a) Initial specimen at 650 °C; (b) WR-300 specimen at 650 °C; (c) WR-400 specimen at 650 °C; (d) WR-500 specimen at 650 °C; (e) Initial specimen at 750 °C; (f) WR-300 specimen at 750 °C; (g) WR-400 specimen at 750 °C; (h) WR-500 specimen at 750 °C

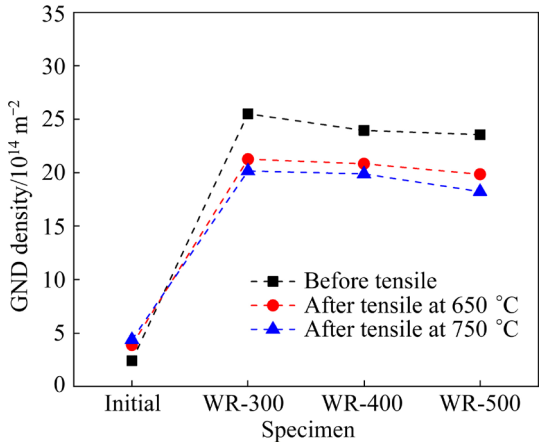

Fig. 9 GND density statistics of initial and warm-rolled specimens

SFs that sheared the γ matrix and γ' phases, accompanied by the formation of L−C locks. In addition, a large quantity of SFs and dislocations were observed in the annealing twins and matrix, and TBs hindered the expansion of SFs and the movement of dislocations, as shown in Fig. 10(a_2). In contrast, many deformation nano-twins sheared the γ matrix and γ' phases in the WR-300 specimen tested at 650 °C, as shown in Fig. 10(b) and its inset. This result indicated that the deformation of the WR-300 specimen tested at 650 °C was dominated by deformation nano-twins that sheared the γ matrix and γ' phases. Furthermore, high-density SFs and L−C locks were observed on both sides of the deformation nano-twins (Fig. 10(b_1)) in this specimen, and the intersection between the deformed nano-twins and SFs shown in the corresponding FFT image (Fig. 10(b_2)) suggested that the formation of deformation nano-twins under thermal-mechanical coupling was caused by the transition of the L−C locks [31].

When tested at 750 °C, various paired dislocations shearing the γ matrix and γ' phases were observed inside the slip bands of the initial specimen, as shown in Fig. 10(c). Furthermore, a considerable quantity of bowing dislocations and dislocation loops were clearly observed in the vicinity of the γ' phases (Fig. 10(c) and its inset), a few deformation nano-twins sheared the γ matrix and γ' phases (Fig. 10(c_1) and its inset), and many dislocations and SFs accumulated near the annealing TBs (Fig. 10(c_2)). These results indicated that the deformation of the initial specimen tested at 750 °C was dominated by dislocation pairs and deformation nano-twins shearing the γ matrix and γ' phases as well as dislocations bypassing the γ' phase. In contrast, a large quantity of deformation nano-twins shearing the γ matrix and γ' phases were observed in the WR-300 specimen tested at 750 °C, as shown in Figs. 10(d, d_1). Furthermore, a large quantity of deformation nano-twins in the same

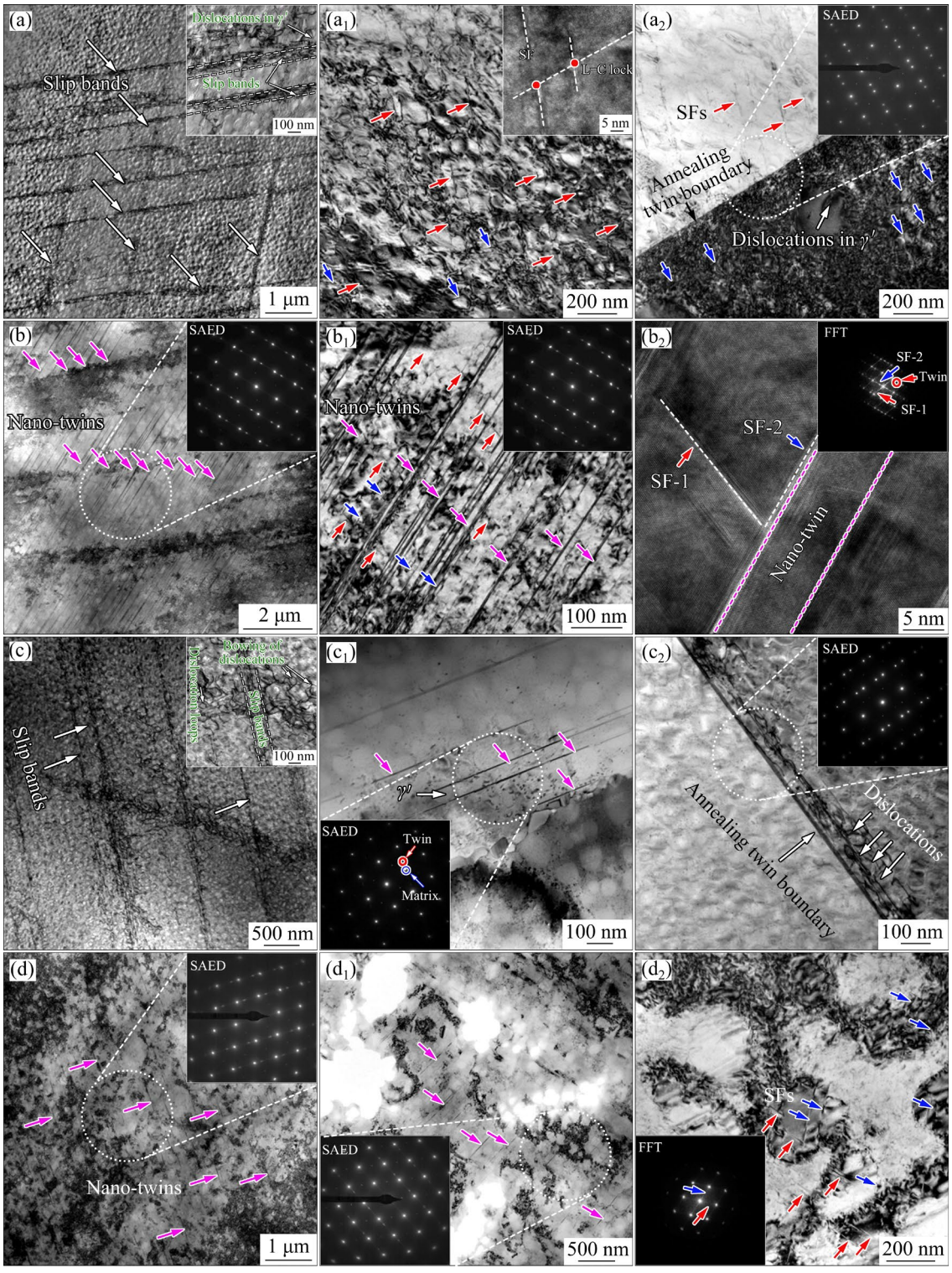

Fig. 10 TEM and HRTEM images showing deformation mechanisms for initial and WR-300 specimens at different deformation temperatures: (a, a_1, a_2) Initial specimen at 650 °C; (b, b_1, b_2) WR-300 specimen at 650 °C; (c, c_1, c_2) Initial specimen at 750 °C; (d, d_1, d_2) WR-300 specimen at 750 °C

grain were parallel to each other (Figs. 10(d, d_1)), and there were numerous SFs and L−C locks in the deformed grains (Fig. 10(d_2)). These results indicated that the deformation mechanism of the WR-300 specimen tested at 750 °C was similar to that of the same specimen tested at 650 °C, which was dominated by deformation nano-twins shearing the γ matrix and γ' phases.

4 Discussion

4.1 Formation mechanisms of SFs and L−C locks

The results of the experiments conducted in this study clearly indicated that high-density SFs and L−C locks were formed in the considered alloy by WR deformation at 300−500 °C and intermediate-temperature tensile deformation. Generally, SFs are believed to result from the slip of Shockley partial dislocations with a Burgers number of $a/6\langle 112\rangle$ on the {111} plane [32]. That is, the formation of SFs is closely related to the formation of extended dislocations. Typically, in face-centred cubic metals, a perfect dislocation with a Burgers number of $a/2\langle 110\rangle$ is dissociated into two Shockley partial dislocations separated by a SF called an extended dislocation [33,34]. The TEM and HRTEM observations of the WR specimens at different temperatures (Figs. 3(c−i)) indicated that WR induced high-density SFs in the γ matrix or/and γ' phase of the alloy. To further analyze the formation mechanisms of these SFs, the nonintersecting SFs were characterized through HRTEM, as shown in Figs. 11(a, b). Figure 11(a) clearly shows that the SFs on the two {111} planes have not yet intersected; Fig. 11(b) shows the HRTEM image of a typical SF in a WR specimen, clearly showing that a perfect $a/2[\bar{1}10]$ dislocation was dissociated into Shockley partial dislocations of $a/6[\bar{1}2\bar{1}]$ and $a/6[\bar{2}11]$ separated by a SF on the (111) slip plane, as expressed by [35]

$$a/2[\bar{1}10]\rightarrow a/6[\bar{1}2\bar{1}]+\mathrm{SF}+a/6[\bar{2}11] \quad (1)$$

In addition, high-density L−C locks were formed by intersecting SFs in the alloys subjected to WR deformation (Figs. 3(c−i)) and intermediate-temperature tensile deformation (Fig. 10). A L−C lock comprises two SFs connected by a stair-rod dislocation. Generally, a L−C lock is formed by reactions between Shockley partial dislocations enclosing intersecting SFs on different {111} slip planes [36]. To further analyze the formation mechanisms of L–C locks in the considered alloy, the intersecting SFs on two different {111} planes were characterized through HRTEM, as shown in Figs. 11(c−e). Figure 11(c) and the corresponding FFT in Fig. 11(d) show that numerous intersecting SFs are activated on the two {111} slip planes of the alloy, leading to the formation of L–C locks. During the WR deformation or intermediate-temperature tensile deformation of the alloy, two perfect dislocations with Burgers numbers of $a/2[\bar{1}01]$ and $a/2[011]$ dissociated into extended dislocations on their respective slip planes of (111) and $(1\bar{1}\bar{1})$. These dislocation reactions can be expressed as follows:

For (111) plane:

$$a/2[\bar{1}01]\rightarrow a/6[\bar{2}11]+\mathrm{SF\text{-}2}+a/6[11\bar{2}] \quad (2)$$

For $(1\bar{1}\bar{1})$ plane:

$$a/2[001]\rightarrow a/6[112]+\mathrm{SF\text{-}1}+a/6[\bar{1}21] \quad (3)$$

When two leading Shockley partial dislocations slip to the conjugate planes, they encounter two slip planes to form a sessile stair-rod dislocation via the following dislocation reaction:

$$a/6[2\bar{1}\bar{1}]+a/6[\bar{1}21]\rightarrow a/6[110] \quad (4)$$

Therefore, the dislocation configuration formed by three partial dislocations and two SFs on the angular plane between two {111} planes is called the L−C lock, as shown in Fig. 11(e). As the tensile deformation temperature increases, L−C locks are more likely to transform into DTs in Ni-based superalloys [31]. The TEM and HRTEM observations (Figs. 10(b, b_1, b_2) and (d, d_1, d_2) of the WR-300 specimens during tensile deformation at 650 and 750 °C confirmed that a larger quantity of deformed nano-twins were formed in the alloy by the transition of L−C locks.

4.2 Contribution of SFs to intermediate-temperature strength and ductility

The results of this study indicated that the high-density SFs induced in the Ni-based wrought superalloy by WR made three critical contributions to the simultaneous improvement of its intermediate-temperature strength and ductility. Firstly, the contribution of pre-existing high-density SFs to the intermediate-temperature strength and ductility of the alloy is closely related to the thermal stability of the SFs and the interaction between SFs and dislocations. WANG et al [37] reported that the SFs in the Al−7.5Y (wt.%) alloy were thermally stable at temperatures up to 400 °C, although their fraction likely decreased with increasing temperature. BEZOLD et al [38] found that the high-density SFs in the Ni−Co-based superalloy remained after annealing at 900 °C for 100 h, indicating that the SFs had excellent thermal stability below this temperature. Furthermore, the strengthening of the

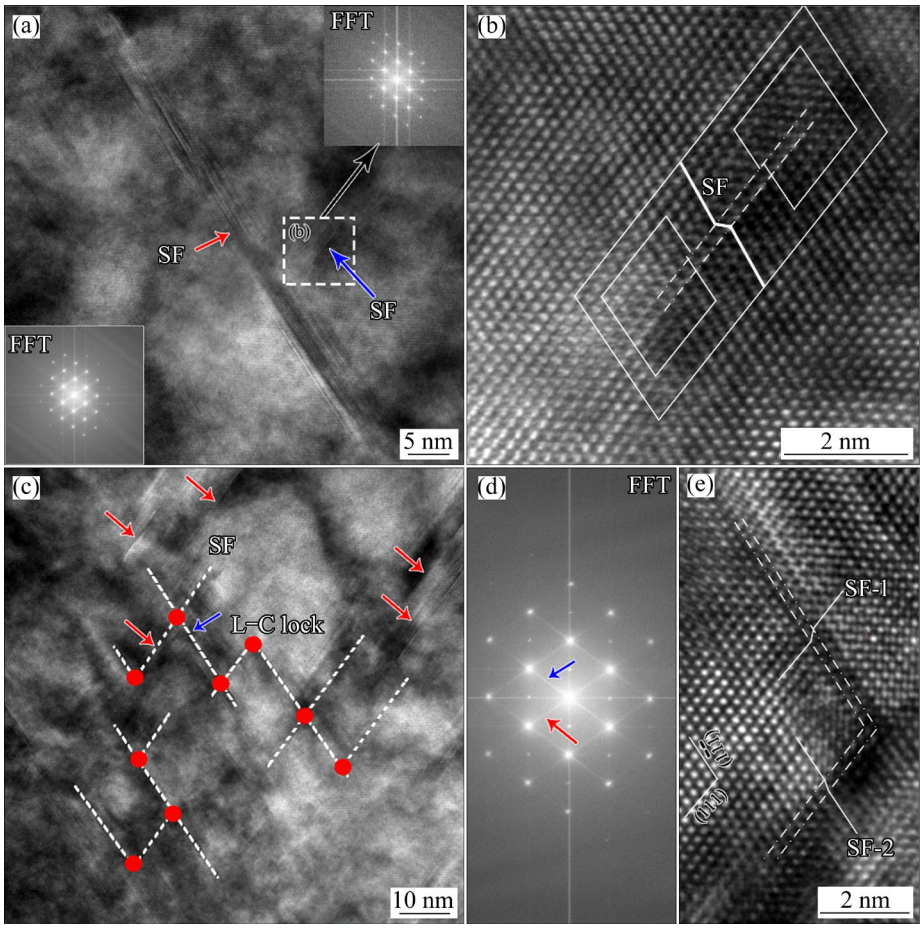

Fig. 11 Morphologies of typical SFs and L−C locks: (a) HRTEM image of SFs and corresponding FFT map in WR-400 specimen; (b) Typical HRTEM image of extended dislocation configuration in WR-400 specimen; (c) HRTEM image of L−C locks in WR-500 specimen; (d) FFT map of (c), indicating intersecting SFs on two different {111} planes; (e) Typical HRTEM image of L−C lock configuration in WR-500 specimen

alloy depends on effectively preventing high-density stable SFs from transforming to dislocations, whereas plastic deformation is accommodated by the cross-slip of partial dislocations along the SFs [39−42].

In addition, pre-existing high-density SFs in the alloy may lead to work softening during high-temperature tensile deformation. SU et al [30] studied the deformation mechanism of face-centered cubic Co dominated by high-density SFs using molecular dynamics and reported that the work softening phenomenon at low strain rates arose from an insufficient density of intersections or Hirth locks and the propagation of partial dislocations along SF ribbons, whereas the work hardening phenomenon at high strain rates arose from abundant Hirth locks, and that SF intersections can effectively inhibit the migration of partial dislocations. Secondly, the high-density SFs on intersections of two (111) slip planes in the alloy have been observed to lead to the formation of high-density L−C locks, which act as effective barriers to dislocation migration and lead to work hardening [43−45]. FAN et al [46] reported that deformation-induced hierarchical SF networks and associated high-density L−C locks in a $(Ni_{1.5}FeCoCr_{0.5})_{87.5}Al_{7.5}Ti_{5.0}$ alloy enhanced its work hardening response, leading to a considerable large tensile ductility.

Thirdly, pre-existing high-density SFs in the alloy may form deformation nano-twins during the intermediate-temperature tensile deformation, leading to the simultaneous improvement in its strength and ductility. It is well known that TBs with nanoscale spacings typically exhibit high thermal and mechanical stabilities to impede dislocation motion and enable dislocation slip accumulation, enhancing the strength and plasticity

of an alloy [47−51]. For example, XU et al [8] found that the ultimate tensile strength and uniform elongation of Ni−Co-based superalloys subjected to tension at 650 and 725 °C can be simultaneously improved by decreasing the SF energy to activate micro-twinning deformation. Furthermore, DING et al [52] reported that deformation-induced nano-twins simultaneously enhanced the strength and ductility of the GH3536 alloy at cryogenic temperatures, and TIAN et al [20] reported that deformation micro-twins enhanced the yield strength and strain-hardening ability of a Ni-based disk superalloy at higher temperatures.

Based on this discussion, the simultaneous improvement of strength and plasticity was achieved in the WR alloys tested at 650 and 750 °C by the interaction of pre-existing high-density SFs and L−C locks with dislocations, as well as the formation of deformation nano-twins during tensile loading. This can be summarized as an optimization of the microstructure and deformation mechanism of the alloy by WR deformation. For illustration, WR-300 specimen was taken as an example and shown in Fig. 12, in which the high-density SFs and L−C locks were introduced into the alloy by WR deformation while the morphology and size of the γ' phase remained basically unchanged. Thus, the interaction between the pre-existing high-density SFs and dislocations during intermediate-temperature tensile loading simultaneously improved the strength and plasticity of the alloy. In addition, the pre-existing high-density L−C locks and the L−C locks formed during the intermediate-temperature tensile loading hindered the movement of dislocations, thereby improving the strength of the alloy. Finally, the high-density nano-twins formed during the intermediate-temperature tensile loading simultaneously improved the strength and plasticity of the alloy. Thus, the excellent intermediate-temperature (650 and 750 °C) mechanical properties of all the WR specimens compared to those of the initial specimen can be primarily attributed to the interaction of pre-existing high-density SFs and L−C locks with dislocations as well as to the formation of high-density deformation nano-twins during tensile loading. CAI et al [53] reported that cold-drawing deformation-induced SFs, L–C locks, and nano-twins in the MP159 CoNiCr superalloy contributed to an improvement in strength, and ZHANG et al [54] reported that a NiCoCr-based medium-entropy alloy exhibited superior yield strength and high ductility owing to the synergetic effect of ultra-fine γ' particles, SFs, L−C locks, and DTs.

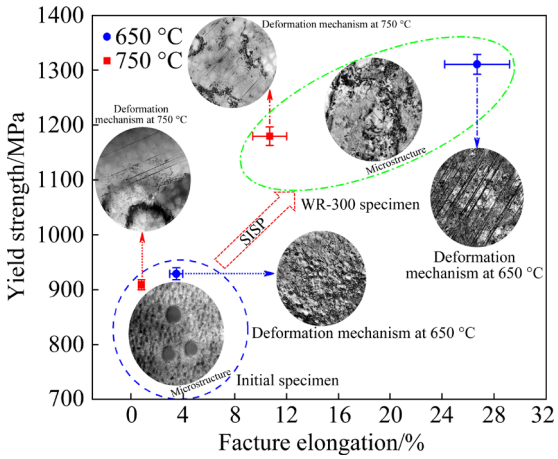

Fig. 12 Synchronous improvement of yield strength and facture elongation of WR-300 specimen at 650 and 750 °C owing to optimization of microstructure and deformation mechanism

5 Conclusions

(1) Compared with the initial specimen, high-density SFs and L−C locks were induced in all the WR specimens through WR deformation. The number of SFs and L−C locks in the alloy increased with the increase of the WR temperature. In addition, the planar SF-dominated deformation mode was observed during WR deformation at 300−500 °C.

(2) Compared with the initial specimen (YS=(929±11) MPa, UTS=(1104±20) MPa, and ε_f=(3.2±0.5)% at 650 °C; YS=(909±9) MPa, UTS=(949±11) MPa, and ε_f=(0.8±0.2)% at 750 °C), the yield strength, ultimate tensile strength, and facture elongation of all the WR specimens increased simultaneously. In particular, the WR-300 specimen exhibited a superior combination of high strength (YS=(1311±18) MPa and UTS=(1462±25) MPa at 650 °C; YS=(1180±17) MPa and UTS=(1293±15) MPa at 750 °C) with high fracture elongation (ε_f=(26.7±2.5)% at 650 °C; ε_f=(10.7±1.3)% at 750 °C).

(3) When tested at 650 °C, the deformation mechanism of the initial specimen was dominated by dislocation pairs and SFs shearing the γ matrix and γ' phases accompanied by the formation of L−C

locks, whereas that of the WR specimens was dominated by deformation nano-twins shearing the γ matrix and γ' phases. However, when tested at 750 °C, the deformation mechanism of the initial specimen was dominated by dislocation pairs and deformation nano-twins shearing the γ matrix and γ' phases as well as dislocations bypassing the γ' phase, whereas that of the WR specimens was still dominated by deformation nano-twins shearing the γ matrix and γ' phases.

(4) The high strength and large facture elongation of all the WR specimens tested at 650 and 750 °C were primarily attributed to the interaction of pre-existing γ' phases, high-density SFs and L−C locks with dislocations as well as to the formation of high-density deformation nano-twins during tensile loading.

CRediT authorship contribution statement

Yu-bi GAO: Investigation, Writing – Original draft, Writing – Review & editing; **Xing-mao WANG:** Data curation, Formal analysis, Writing – Review & editing; **Jia-yu XU:** Data curation, Writing – Review & editing; **Bo LIU:** Investigation, Validation, Visualization; **Bing ZHEN:** Investigation, Validation, Visualization; **Yu-tian DING:** Conceptualization, Methodology, Supervision, Funding acquisition; **Bin GAN:** Conceptualization, Methodology, Supervision; **Ting-biao GUO:** Funding acquisition; **Jun-zhao LIU:** Funding acquisition.

Declaration of competing interest

The authors declare that they have no known competing financial interests or personal relationships that could have appeared to influence the work reported in this paper.

Acknowledgments

This work was financially supported by the Program for Hong Liu Excellent Young Scholars by Lanzhou University of Technology in 2023, the National Key Research and Development Program of China (No. 2017YFA0700703), the Major Science and Technology Project of Gansu Province, China (Nos. 22ZD6GA008, 23ZDGC002, 23ZDGA010), the Gansu Provincial Key Research and Development Program, China (No. 20YF3GA041), and the Special Fund of National Key Laboratory of Ni&Co Associated Minerals Resources Development and Comprehensive Utilization by Jinchuan Group Co., Ltd., China (No. GZSYS-KY-2022-012).

References

[1] REED R C. The superalloys: Fundamentals and applications [M]. Cambridge: Cambridge University Press, 2006.

[2] POLLOCK T M. Alloy design for aircraft engines [J]. Nature Materials, 2016, 15: 809−815.

[3] ZHANG Peng, ZHU Qiang, CHEN Gang, QIN He-yong, WANG Chuan-jie. Grain size based low cycle fatigue life prediction model for nickel-based superalloy [J]. Transactions of Nonferrous Metals Society of China, 2018, 28(10): 2102−2106.

[4] LI Fang, YUAN Ding-ling, CHNE Kang-hua, CHEN Song-yi, LI Li. A novel creep model with synergetic Orowan bypassing and climbing mechanisms in nickel-base superalloys [J]. Transactions of Nonferrous Metals Society of China, 2024, 34(4): 1167−1177.

[5] HE L Z, ZHENG Q, SUN X F, HOU G C, GUAN H R, HU Z Q. Low ductility at intermediate temperature of Ni-base superalloy M963 [J]. Materials Science and Engineering: A, 2004, 380: 340−348.

[6] ZHENG L, SCHMITZ G, MENG Y, CHELLALI R, SCHLESIGER R. Mechanism of intermediate temperature embrittlement of Ni and Ni-based superalloys [J]. Critical Reviews in Solid State & Materials Sciences, 2012, 37: 181−214.

[7] JIANG L, YE X X, CUI C Y, HUANG H F, LENG B, LI Z J, ZHOU X T. Intermediate temperature embrittlement of one new Ni−26W−6Cr based superalloy for molten salt reactors [J]. Materials Science and Engineering: A, 2016, 668: 137−145.

[8] XU H, ZHANG Z J, ZHANG P, CUI C Y, JIN T, ZHANG Z F. The synchronous improvement of strength and plasticity (SISP) in new Ni−Co based disc superalloys by controlling stacking fault energy [J]. Scientific Reports, 2017, 7(1): 8046.

[9] TANG L, LIANG J J, CUI C Y, LI J G, ZHOU Y Z, SUN X F, DING Y T. Influence of Co content on the microstructures and mechanical properties of a Ni−Co base superalloy made by specific additive manufacturing process [J]. Materials Science and Engineering: A, 2020, 786: 139438.

[10] YANG C L, ZHANG Z J, ZHANG P, CUI C Y, ZHANG Z F. Synchronous improvement of the strength and plasticity of Ni−Co based superalloys [J]. Materials Science and Engineering: A, 2018, 736: 100−104.

[11] ZHU C Z, ZHANG R, CUI C Y, ZHOU Y Z, YUAN Y, YU Z S, LIU X, SUN X F. Effect of Ta addition on the microstructure and tensile properties of a Ni−Co base superalloy [J]. Metallurgical and Materials Transactions A, 2021, 52: 108−118.

[12] LIU P, ZHANG R, YUAN Y, CUI C Y, LIANG F G, LIU X, GU Y F, ZHOU Y Z, SUN X F. Effects of nitrogen content on microstructures and tensile properties of a new Ni−Fe based wrought superalloy [J]. Materials Science and Engineering: A, 2021, 801: 140436.

[13] PU E X, ZHENG W J, SONG Z G, ZHANG K, LIU S, SHEN W X, DONG H. The effect of aging on the serrated yielding and intermediate temperature embrittlement of

nickel-base C-276 alloy [J]. Materials Science and Engineering: A, 2018, 714: 59−67.

[14] BAI Y B, ZHANG R, CUI C Y, ZHOU Y Z, SUN X F. Eliminating embrittlement of GH4065A superalloy at intermediate temperature by a novel grain boundary strengthening mechanism [J]. Materials Letters, 2023, 335: 133789.

[15] YANG T, ZHAO Y L, FAN L, WEI J, LUAN J H, LIU W H, WANG C, JIAO Z B, KAI J J, LIU C T. Control of nanoscale precipitation and elimination of intermediate-temperature embrittlement in multicomponent high-entropy alloys [J]. Acta Materialia, 2020, 189: 47−59.

[16] PAN Y W, DONG A P, ZHOU Y, ANTONOV S, CHEN Z F, DU D F, SUN B D. Synergistic enhancement of high temperature strength and ductility with a novel γ/ε dual-phase hetero-nanostructure in NiCoCr-based alloys [J]. Materials Science and Engineering: A, 2023, 877: 145142.

[17] YOU Z Y, TANG Z Y, CHU F B, DING H, MISRA R D K. Significantly enhancing elevated-temperature strength and ductility of a FeMnCoCr high-entropy alloy via grain boundary engineering: Exploring multi-deformation mechanisms [J]. Materials Science and Engineering: A, 2023, 886: 145547.

[18] GUAN X J, SHI F, JI H M, LI X W. A possibility to synchronously improve the high-temperature strength and ductility in face-centered cubic metals through grain boundary engineering [J]. Scripta Materialia, 2020, 187: 216−220.

[19] YUAN Y, GU Y F, ZHONG Z H, YOKOKAWA T, HARADA H. Enhanced strength at intermediate temperatures in a Ni-base disk superalloy with high Co addition [J]. Materials Science and Engineering: A, 2012, 556: 595−600.

[20] TIAN C G, HAN G M, CUI C Y, SUN X F. Effects of Co content on tensile properties and deformation behaviors of Ni-based disk superalloys at different temperatures [J]. Materials & Design, 2015, 88: 123−131.

[21] ZHU C Z, ZHANG R, CUI C Y, ZHOU Y Z, QU J L, GAN B, ZHANG B J, SUN X F. Effect of pre-strain treatment on mechanical properties of a Ni−Co base disk superalloy [J]. Journal of Alloys and Compounds, 2022, 905: 164167.

[22] YANG C, HU R, WANG X M, DU J H, LUO X, BI Z N, GAN B. Effect of pre-tensile treatments on the mechanical properties and deformation mechanism of a novel Ni-based superalloy [J]. Materials Science and Engineering: A, 2023, 874: 145063.

[23] WANG X M, DING Y T, YU H Y, BI Z N, GAO Y B, GAN B. High strength and ductility in a novel Ni-based superalloy with γ' and nanotwins/stacking faults architectures [J]. Materials Science and Engineering: A, 2022, 847: 143293.

[24] WANG W, LARTIGUE-KORINEK S, BRISSET F, HELBERT A L, BOURGON J, BAUDIN T. Formation of annealing twins during primary recrystallization of two low stacking fault energy Ni-based alloys [J]. Journal of Materials Science, 2015, 50: 2167−2177.

[25] GAO Y B, DING Y T, MA Y J, CHEN J J, WANG X M, XU J Y. Evolution of annealing twins in Inconel 625 alloy during tensile loading [J]. Materials Science and Engineering: A, 2022, 831: 142188.

[26] Academic Committee of the Superalloys, CSM. Chain superalloys handbook (Book 1) [M]. Beijing: Standards Press of China, 2012. (in Chinese)

[27] ZHAO Guang-pu, HUANG Shuo, ZHANG Bei-jiang, XU Guo-hua, QIN He-yong, ZHANG Wen-yun. Microstructure control and mechanical properties of the newest nick-based wrought superalloy GH4065A [J]. Journal of Iron and Steel Research, 2015, 27(2): 37−44.

[28] ZHANG W Y, HUANG S, TIAN Q, QING H Y, XU G H, ZHAO G P, ZHANG B J. Microstructure control and mechanical properties of new developed C&W superalloy GH4175 at 800 °C [J]. IOP Conference Series: Materials Science and Engineering, 2018, 452: 022123.

[29] CUI Chuan-yong, BAI Ying-bo, ZHANG Rui, ZHOU Zi-jian, ZHOU Yi-zhou, SUN Xiao-feng. Study on forming process and mechanical properties of GH4068 alloy pipe [J]. Aeronautical Manufacturing Technology, 2022, 65(10): 36−43. (in Chinese)

[30] SU R, NEFFATI D, XUE S, LI Q, FAN Z, LIU Y, WANG H, KULKARNI Y, ZHANG X. Deformation mechanisms in FCC Co dominated by high-density stacking faults [J]. Materials Science and Engineering: A, 2018, 736: 12−21.

[31] QI D Q, FU B D, DU K, YAO T T, CUI C Y, ZHANG J X, YE H Q. Temperature effects on the transition from Lomer−Cottrell locks to deformation twinning in a Ni−Co-based superalloy [J]. Scripta Materialia, 2016, 125: 24−28.

[32] WU X, ZHU Y T, CHEN M W, MA E. Twinning and stacking fault formation during tensile deformation of nanocrystalline Ni [J]. Scripta Materialia, 2006, 54: 1685−1690.

[33] YUAN Y, GU Y F, CUI C Y, OSADA T, YOKOKAWA T, HARADA H. A novel strategy for the design of advanced engineering alloys: Strengthening turbine disk superalloys via twinning structures [J]. Advanced Engineering Materials, 2011, 13: 296−300.

[34] GAO Y B, DING Y T, LI H F, DONG H B, ZHANG R Y, LI J, LUO Q S. Grain-size dependent elastic-plastic deformation behaviour of Inconel 625 alloy studied by in-situ neutron diffraction [J]. Intermetallics, 2021, 138: 107340.

[35] XU Y J, QI D Q, DU K, CUI C Y, YE H Q. Stacking fault effects on dynamic strain aging in a Ni−Co-based superalloy [J]. Scripta Materialia, 2014, 87: 37−40.

[36] YAN Z G, LIN Y J. Lomer−Cottrell locks with multiple stair-rod dislocations in a nanostructured Al alloy processed by severe plastic deformation [J]. Materials Science and Engineering: A, 2019, 747: 177−184.

[37] WANG M M, KNEZEVIC M, CHEN M, LI J S, LIU T, WANG G, ZHAO Y, WANG M, LIU Q, HUANG Z J, DU D F, GAO H Y, WANG J, SUN B D. Microstructure design to achieve optimal strength, thermal stability, and electrical conductivity of Al−7.5wt.%Y alloy [J]. Materials Science and Engineering: A, 2022, 852: 143700.

[38] BEZOLD A, AMON L, KARPSTEIN N, SPIECKER E, GÖKEN M, NEUMEIER S. Recovery of superlattice stacking faults at high temperatures [J]. Scripta Materialia, 2023, 222: 115005.

[39] WEI H J, WEI Y G. Interaction between a screw dislocation and stacking faults in FCC metals [J]. Materials Science and

Engineering: A, 2012, 541: 38−44.
[40] JIAN W W, CHENG G M, XU W Z, KOCH C C, WANG Q D, ZHU Y T, MATHAUDHU S N. Physics and model of strengthening by parallel stacking faults [J]. Applied Physics Letters, 2013, 103: 133108.
[41] LIU Y, CHEN Y, YU K Y, WANG H, CHEN J, ZHANG X. Stacking fault and partial dislocation dominated strengthening mechanisms in highly textured Cu/Co multilayers [J]. International Journal of Plasticity, 2013, 49: 152−163.
[42] SU R Z, NEFFATI D, ZHANG Y F, ZHAO J, LI J, WANG H Y, KULKARNI Y, ZHANG X H. The influence of stacking faults on mechanical behavior of advanced materials [J]. Materials Science and Engineering: A, 2021, 803: 140696.
[43] WU X L, ZHU Y T, WEI Y G, WEI Q. Strong strain hardening in nanocrystalline nickel [J]. Physical Review Letters, 2009, 103: 205504.
[44] LEE J H, HOLLAND T B, MUKHERJEE A K, ZHANG X H, WANG H Y. Direct observation of Lomer−Cottrell locks during strain hardening in nanocrystalline nickel by in situ TEM [J]. Scientific Reports, 2013, 3: 1061.
[45] CHEN S J, OH H S, GLUDOVATZ B, KIM S J, PARK E S, ZHANG Z, RITCHIE R O, YU Q. Real-time observations of TRIP-induced ultrahigh strain hardening in a dual-phase CrMnFeCoNi high-entropy alloy [J]. Nature Communications, 2020, 11: 826.
[46] FAN L, YANG T, ZHAO Y L, LUAN J H, ZHOU G, WANG H, JIAO Z B, LIU C T. Ultrahigh strength and ductility in newly developed materials with coherent nanolamellar architectures [J]. Nature Communications, 2020, 11: 6240.
[47] LU L, SHEN Y F, CHEN X H, QIAN L H, LU K. Ultrahigh strength and high electrical conductivity in copper [J]. Science, 2004, 304: 422−426.
[48] LU L, CHEN X, HUANG X, LU K. Revealing the maximum strength in nanotwinned copper [J]. Science, 2009, 323: 607−610.
[49] LU K. Stabilizing nanostructures in metals using grain and twin boundary architectures [J]. Nature Reviews Materials, 2016, 1: 16019.
[50] WANG Z J, LI Q J, LI Y, HUANG L C, LU L, DAO M, LI J, MA E, SURESH S, SHAN Z W. Sliding of coherent twin boundaries [J]. Nature Communications, 2017, 8: 1108−1115.
[51] GAO Y B, DING Y T, CHEN J J, XU J Y, MA Y J, WANG X M. Effect of twin boundaries on the microstructure and mechanical properties of Inconel 625 alloy [J]. Materials Science and Engineering: A, 2019, 767: 138361.
[52] DING Q, BEI H, WEI X, GAO Y F, ZHANG Z. Nano-twin-induced exceptionally superior cryogenic mechanical properties of a Ni-based GH3536 (Hastelloy X) superalloy [J]. Materials Today Nano, 2021, 14:100110.
[53] CAI Y Q, TAN Y B, WANG L X, SHI W, JI X M, XIANG S. Multiple strengthening mechanisms induced by nanotwins and stacking faults in CoNiCr-superalloy MP159 [J]. Materials Science and Engineering: A, 2022, 853: 143793.
[54] ZHANG L, HU Z H, ZHANG L, WANG H, LI J B, LI Z, YU J X, WU B L. Enhancing the strength−ductility trade-off in a NiCoCr-based medium-entropy alloy with the synergetic effect of ultra fine precipitates, stacking faults, dislocation locks and twins [J]. Scripta Materialia, 2022, 211: 114497.

通过高密度层错调控协同提高镍钴基高温合金的中温强度和塑性

高钰璧[1,2]，王兴茂[1,2]，许佳玉[1,2]，刘 博[1,2]，
甄 炳[1,2]，丁雨田[1,2]，甘 斌[3]，郭廷彪[1,2]，刘俊钊[1,2]

1. 兰州理工大学 材料科学与工程学院，兰州 730050；
2. 兰州理工大学 省部共建有色金属先进加工与再利用国家重点实验室，兰州 730050；
3. 钢铁研究总院 高温合金新材料北京市重点实验室，北京 100081

摘 要：通过 300~500 ℃的温轧变形将高密度层错引入一种新型镍钴基高温合金中，并研究其对合金中温(650 ℃和 750 ℃)拉伸性能的影响。结果表明，与原始试样相比，所有温轧试样具有高密度的层错和 Lomer−Cottrell 锁。同时，高密度层错使合金的中温强度和塑性得到协同提高。特别是，300 ℃温轧试样表现出优异的高强度(650 ℃时屈服强度和极限抗拉强度分别为(1311±18)和(1462±25) MPa，750 ℃时分别为(1180±17) MPa 和(1293±15) MPa)和高断裂伸长率(650 ℃时为(26.7±2.5)%，750 ℃时为(10.7±1.3)%)组合。所有温轧试样的高强度和高断裂伸长率主要归因于预先存在的 γ'相、高密度层错和 Lomer−Cottrell 锁与位错的交互作用以及拉伸加载过程中高密度变形纳米孪晶的形成。

关键词：镍钴基高温合金；温轧；层错；Lomer−Cottrell 锁；变形纳米孪晶；力学性能

(Edited by Wei-ping CHEN)